ADVANCED FUNCTIONAL MATERIALS
www.afm-journal.de

High-Rate FA-Based Co-Evaporated Perovskites: Understanding Rate Limitations and Practical Considerations to Overcome Their Impact

Thomas Feeney, Aleksandra Miaskiewicz, Julian Petry, Felix Laufer, Roja Singh, Stefanie Severin, Viktor Škorjanc, Alexander Diercks, Suresh Maniyarasu, Lars Korte, Steve Albrecht,* Ulrich W. Paetzold,* Marcel Roß,* and Paul Fassl**

Vapor phase deposition methods are readily able to achieve uniform coverage of large-area substrates and are widely considered promising for industrial-scale perovskite solar cell fabrication. However, as perovskite-silicon tandem solar cells approach commercialization, practical considerations of manufacturing throughput come into play. Here, it is shown that the inherent sublimation characteristics of the organic precursor formamidinium iodide (FAI) make increasing the deposition rate of FA-based co-evaporated perovskites negatively impact replicability and lead to a substantial decrease in power conversion efficiency (PCE). These losses are linked to reduced film homogeneity and the emergence of carbon-rich regions within the perovskite layer. To mitigate these rate-induced effects, two approaches are explored: source layout optimization and material preconditioning. Utilizing dual FAI sources rather than a single FAI source reduces the relative PCE drop from ≈23%$_{rel}$ to ≈9%$_{rel}$ at a deposition rate of ≈18 nm min^{-1} (14.8% PCE @ maximum power point (MPP)) compared to the baseline rate of 5 nm min^{-1} (16.2% PCE @MPP). Alternatively, preconditioning a single FAI source reduces the performance losses from ≈31%$_{rel}$ to ≈26%$_{rel}$ at a deposition rate of ≈21 nm min^{-1}. These findings underscore the importance of tailored source strategies to enable high-rate FA-based co-evaporated perovskites without compromising device performance.

1. Introduction

Organic–inorganic metal halide perovskite solar cells (PSCs) are a promising class of photovoltaic devices, owing to their excellent optoelectronic properties coupled with versatile fabrication methods and low fabrication costs.[1–3] Utilizing formamidinium (FA) halides as organic precursor are particularly promising due to their enhanced operational stability, which is a concern for perovskite commercialization.[4–7] Furthermore, wide bandgap (≥1.65 eV) perovskites with the *p-i-n* architecture can be readily incorporated into a wide variety of tandem devices,[8–10] which are a crucial next step in increasing power conversion efficiencies (PCEs).[11,12]

Absorber fabrication for PSCs can be broadly divided into two classes: solution-based and vacuum-based vapor-phase processes. Solution processing encompasses spin coating, inkjet printing, slot-die coating, and spray coating, offering simple

T. Feeney, F. Laufer, R. Singh, A. Diercks, U. W. Paetzold, P. Fassl
Light Technology Institute
Karlsruhe Institute of Technology (KIT)
Engesserstraße 13, 76131 Karlsruhe, Baden-Württemberg, Germany
E-mail: thomas.feeney@kit.edu; ulrich.paetzold@kit.edu; paul.fassl@kit.edu

A. Miaskiewicz, S. Severin, V. Škorjanc, S. Maniyarasu, L. Korte, S. Albrecht, M. Roß
Helmholtz Zentrum Berlin (HZB) Solar Energy Division
Kekuléstraße 5, 12489 Berlin, Berlin, Germany
E-mail: steve.albrecht@helmholtz-berlin.de; marcel.ross@helmholtz-berlin.de

The ORCID identification number(s) for the author(s) of this article can be found under https://doi.org/10.1002/adfm.202517873

J. Petry, R. Singh, U. W. Paetzold, P. Fassl
Institute of Microstructure Technology
Karlsruhe Institute of Technology (KIT)
Hermann-von-Helmholtz-Platz 1, 76344 Eggenstein-Leopoldshafen, Baden-Württemberg, Germany

S. Albrecht
Faculty of Electrical Engineering and Computer Science
Technical University Berlin
Marchstraße 23, 10587 Berlin, Germany

DOI: 10.1002/adfm.202517873

process optimization and rapid absorber deposition.[13] Vapor phase deposition methods include thermal sublimation from a crucible,[14–17] flash sublimation,[18] magnetron sputtering,[19] laser deposition methods,[20] close-space sublimation,[21] and chemical vapor deposition.[22] Hybrid methods, using a combination of vapor phase deposition and solution processing are also a promising approach.[23,24] Vapor-phase methods are typically well suited for textured surfaces due to their conformal coating properties[16,23,25] and easy thickness control,[15,26] with reduced upscaling losses for industrially relevant active areas.[27–29] Simultaneous thermal sublimation from multiple crucibles is also known as co-evaporation due to semantic drift, and is the current most common vapor-phase method.

The industrial relevance of each fabrication class remains uncertain.[30] Solution-based methods are prone to higher upscaling losses,[27] can have problems with process repeatability,[31,32] and typically require toxic solvents that render them less appealing for industrial-scale deposition.[33,34] Three issues restrict vacuum-based processes: i) industrial-scale deposition of common vapor phase deposition methods will require a transition to linear evaporation sources, which may result in new deposition challenges;[35] ii) the device performance of *p-i-n* architectures is typically reduced compared to solution-based processes, especially for co-evaporated PSCs. This is usually attributed to poorer charge extraction properties, which reduce device short-circuit current densities (J_{SC}), as well as to the limited options for bulk and surface passivation limiting device open-circuit voltage (V_{OC}),[30] a field that has received significant recent attention;[36–39] iii) vapor-phase processes demonstrate deposition rates well below industrial relevance, with cost modeling predicting deposition rates of ≈1000 nm min^{-1} as necessary to compete with solution-processed processes.[30] While flash sublimation has demonstrated deposition rates above 1000 nm min^{-1}, it remains relatively unexplored and the feasibility of transferring such lab-scale processes to commercial deposition conditions is uncertain.[40,41] The more common process of co-evaporation from crucibles in high vacuum is viable for the deposition of organic light-emitting diodes or copper indium gallium selenide solar cells,[42,43] but in the context of perovskites is a comparatively slow process, with typical FA-based deposition rates below 6 nm min^{-1}.[30] Recent studies on $MAPbI_3$ have aimed to increase deposition speed without compromising PCE, with maximum deposition rates of ≈26 nm min^{-1} achieved.[44,45] However, some MA-based perovskites exhibit a degree of inherent instability under simultaneous light and thermal exposure that renders research into the rate-upscaling of alternative compositions desirable.[46,47] Table S1 (Supporting Information) outlines relevant achieved co-evaporated rates and performances for FA-based and FAMA-based perovskites, in addition to a selection of high-rate or high-PCE MA-based co-evaporated perovskites.

In this work, we explore the limitations associated with increasing the deposition rate of wide bandgap FA-based co-evaporated absorbers suitable for incorporation into tandem photovoltaics, and methods to overcome them. We demonstrate that increasing deposition rate leads to a significant drop in PCE and a notable decrease in repeatability. Mass spectrometry (MS) during baseline and high-rate processes confirms that the studied rates do not significantly impact the vacuum prevalence of common FAI degradation products during deposition.[48] To evaluate performance losses, rate-dependent bulk properties of perovskite films are explored via a combination of photoluminescence (PL) mapping, X-ray diffraction (XRD), and dispersive X-ray spectroscopy (EDX). High deposition rates do not lead to a noticeable change in bulk perovskite composition or bandgap, but are associated with the emergence of carbon-rich inhomogeneities on the perovskite surface. Furthermore, the higher process pressure caused by FAI degradation products leads to a decrease in process repeatability and changes in film formation, although the impact on performance is not clear. A combination of solution-based nuclear magnetic resonance (NMR) and X-ray photoelectron spectroscopy (XPS) indicates significant rate-dependent changes in FAI residual crucible material, which can be correlated to changes in the evaporated material.[35]

To overcome this problem, we demonstrate that utilizing a second FAI source at elevated deposition rates leads to an improvement in sample uniformity, performance, and repeatability compared to single FAI source perovskite depositions at the same rate. We demonstrate that this impact of deposition rate on performance is replicable across research groups, and that crucible shape and preconditioning of the organic cation are also critical to maintain device PCE and uniformity.

To the best of our knowledge, this is the first work to evaluate and explain the effects of deposition rate on the performance of wide bandgap FA-based co-evaporated PSCs. As perovskites increasingly move into the realm of industry, our work provides a framework for challenges and strategies in transferring co-evaporation processes to compatible deposition rates.

2. Results and Discussion

This work comprises depositions by co-evaporation at two different research laboratories, referred to as Process A (KIT, Karlsruhe) and Process B (HZB, Berlin). The reactors for each process are PEROvap systems, however, Process A utilizes 8 cm^3 conical crucibles with a molybdenum heating element, while Process B utilizes 2 cm^3 cylindrical crucibles with a heating block. Both processes employ unwashed spin-coated MeO-2PACz as a HTL to ensure similar substrate-cation interactions.[16,25,50] In consideration of potential tandem devices, both processes employ a double cation wide bandgap (1.68 eV) perovskite absorber via co-evaporation from four sources, with the nominal compositions of $Cs_{0.17}FA_{0.83}Pb(I_{0.75}Br_{0.25})_3$ for Process A and $Cs_{0.2}FA_{0.94}Pb(I_{0.94}Br_{0.11})_3$ for Process B. Unless stated otherwise, we employ the inverted *p-i-n* architecture: glass/indium tin oxide (ITO)/MeO-2PACz/perovskite/C_{60}/BCP/X, where X is Au for Process A and Ag for Process B. A complete description of the deposition conditions for both processes is present in the Experimental Section.

In vapor-phase processes, tooling factors and source temperatures can vary depending on the reactor layout, tooling method, and source type. Measured quartz crystal microbalance (QCM) rates are also susceptible to systematic differences in measurement routines, which can be exacerbated when varying deposition rate.[15,48,51] While rates for inorganic perovskite precursors have been shown to scale relatively linearly within the studied range,[45] organic cation deposition rate is often complicated to determine. Furthermore, high rates (and associated high process pressures, see Figure S1, Supporting Information) can

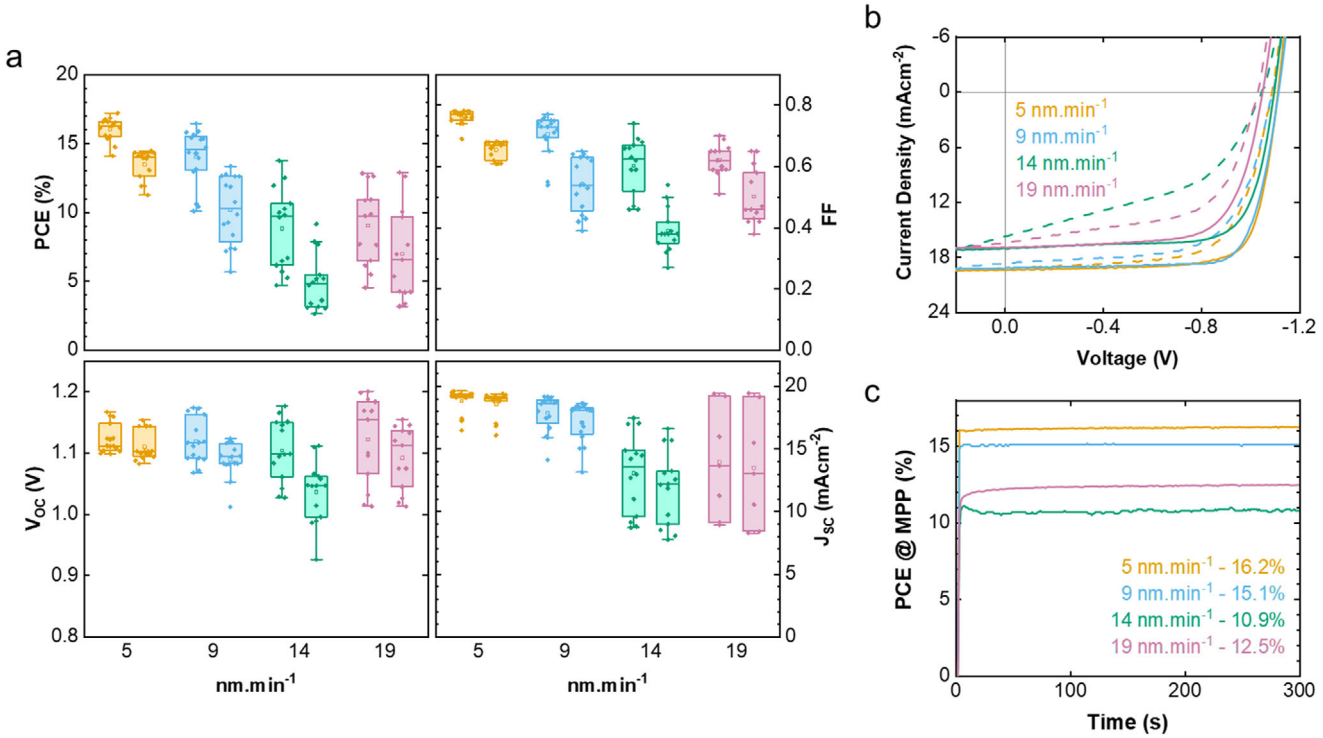

Figure 1. a) Forward and reverse statistics of parameters extracted from *J–V* measurements for champion batches from Process A under perovskite deposition rates ranging from 5 to 19 nm min^{-1}. Also shown are b) *J–V* curves and c) MPP tracking results corresponding to the champion devices from each deposition rate. Each condition shows 4 substrates with typically 4 pixels each (active area 10.5 mm^2).

reduce the mean free path of precursor materials, reducing the overall perovskite deposition rate.[15] A FAI optimization series was performed for a set of constant inorganic deposition rates to avoid non-linear FAI scaling, where the optimum FAI rate may be different depending on the deposition rate. Only the champion batches are shown and selected using champion PCE at maximum power point (MPP). To allow a valid comparison between all processes, we will refer to effective perovskite deposition rate, which was calculated by dividing the final perovskite thickness by the deposition time to obtain a nm min^{-1} rate, which is rounded to the nearest integer. This method prevents apparent changes in deposition rate arising from different perovskite thickness, as seen in literature, where a halving of deposition time corresponds to a less substantial increase in effective rate (≈20 – ≈26 nm min^{-1}) when adjusting for perovskite thickness.[44,45] Hence, nm min^{-1} is the more important figure of merit for upscaling to industrially relevant deposition rates.[30]

2.1. Device Performance Dependence on Rate

To evaluate the impact of deposition rate on co-evaporated *p-i-n* PSCs, we begin by comparing maximum achievable device performances of Process A at rates varying from ≈5 to ≈19 nm min^{-1} without any additional changes in the process. Final thicknesses for champion perovskites were relatively stable in this series at ≈560 ± 20 nm. We do not expect small fluctuations in thickness to significant impact PCE in this thickness range.[52] Additional discussion of our baseline deposition rates, and our methods to ensure process repeatability, are presented in the Experimental Section.

Statistics for the champion PSCs at each deposition rate are provided in **Figure 1a**, along with current density–voltage (*J–V*) curves under standard test conditions (Figure 1b) and MPP tracking of the best-performing devices (Figure 1c). Relevant external quantum efficiency (EQE) measurements are provided in Figure S2 (Supporting Information). Integrated J_{SC} values derived from EQE are within 10% of *J–V* scan values, which is an expected level of deviation.[53,54] At our base deposition rate of 5 nm min^{-1}, the champion device achieved a PCE of 17.2% (fill factor (FF) = 0.78, V_{OC} = 1.12 V, and J_{SC} = 19.6 mA cm^2) in the reverse scan direction. This is broadly comparable to other ≈1.68 eV co-evaporated perovskites,[55,56] although reports of ≥1.65 eV perovskites have surpassed these values using bulk passivation.[36,39] At increased rates, performance steadily decreases, with the champion device deposited at 19 nm min^{-1} displaying a PCE of 12.7% (FF = 0.70, V_{OC} = 1.07 V, and J_{SC} = 16.9 mA cm^{-2}) coupled with significantly increased hysteresis.

Using PCE at MPP values from Figure 1c, with a consistent nominal composition, increasing the rate from 5 to 19 nm min^{-1} leads to a decrease in PCE from 16.2% to 12.5%, corresponding to a 23%$_{rel}$ drop in PCE. We note that the 14 nm min^{-1} champion device exhibited a lower PCE at MPP than the 19 nm min^{-1} champion device. We attribute this i) to higher hysteresis (compare Figure 1b) and ii) to the increased variation of device performance at high rates, which will be discussed in the next paragraph, leading to an anomalously high PCE for the 19 nm min^{-1} champion run. Despite this drop in overall PCE, all champion

devices provide stable power output at MPP for a minimum of 300 s, indicating that high rates do not impact MPP stability. Extended MPP tracking at 25 °C for 250 h also remains relatively stable for every rate (see Figure S3a, Supporting Information), which is in line with previously observed results for other co-evaporated perovskites.[16] We consider it to be an indication that the presented devices are near optimum stoichiometry due to the negative effects of significantly imbalanced stoichiometry on device stability.[6,57–59] This is reinforced by the lack of significant bandgap shift, plotted in Figure S2 (Supporting Information), or a shift in XRD peak positions that will be presented in the next section. We consider the observed differences that will be discussed to be entirely due to changes in deposition rate.

PCE and process repeatability between batches at the same deposition rate is significantly reduced for high-rate processes, with a comparison between several champion 5 and 19 nm min^{-1} batches shown in Figure S4 (Supporting Information). Repeatability can be estimated by considering the coefficient of variation (CV) for a set of samples, which gives a numerical representation of the dispersion around the mean. For 5 nm min^{-1}, the CV_{mean} is 0.094, while for 19 nm min^{-1}, it is 0.195, indicating a significant increase in batch-to-batch variation. FAI rates for the champion devices exhibit a variation of ≈5% in relative FAI rate for 5 nm min^{-1} and ≈10% for 19 nm min^{-1}. This indicates that high rates also show a slight increase in process variability. A potential cause for this drop in repeatability is the substantial variation in process pressure, which leads to a corresponding variation in the mean free path of precursor materials, and impacts precursor flux at the substrate, as outlined in Figure S1 (Supporting Information). This variation in precursor flux is expected to impact perovskite growth.

2.2. Impact on Bulk Perovskite Materials for Each Deposition Rate

Explaining the observed changes in device performance necessitates understanding the rate-dependent changes to bulk perovskite material properties, hence, we undertook an evaluation of half stacks using XRD, PL mapping, and EDX measurements. Comparing each deposition rate, the XRD spectra shown in **Figure 2a** indicate minor diffraction pattern variation. Peak locations were aligned to the ITO peak at ≈35°. While relative (0 0 1), (0 1 1), and (0 1 2) peak intensities shift slightly between samples, as shown in Figure S5 (Supporting Information), no consistent rate-dependent change in overall XRD crystal patterns is observed. The decline in (0 0 1) peak intensity, and increase in other peak intensities, at elevated deposition rates has been observed for various studies of vapor-based perovskites,[20,45] but is not always associated with a decline in device performance. Additional extracted XRD parameters are presented in Table S2 (Supporting Information).

To probe surface uniformity, reflectance and PL mapping of half stacks was conducted for each of the stated rates (Figure 2b). It is important to note that we consider these results qualitative rather than quantitative. PL intensity is normalized for each sample to highlight inhomogeneities and avoid rate-dependent variation. While samples visually appear mostly uniform, seen in the neutral density filter R_{diff} measurements, at high rates there emerges clear evidence of large-scale inhomogeneities in the 725 nm long pass PL maps, i.e., µm-scale dots that exhibit a strongly reduced PL intensity. 775 nm short pass maps show similar inhomogeneities, with a representative comparison shown in Figure S6 (Supporting Information), indicating these inhomogeneities are unlikely to be due to a consistent bandgap shift. To preclude the possibility of sample-dependent variations, multiple substrates from different deposition runs were measured, and the samples presented in Figure 2 are indicative of the typical results. To ensure that substrate inhomogeneity was not a factor, CsCl seed layers were introduced in some samples to reduce the substrate-dependency of the perovskite growth.[36] As shown in Figure S6 (Supporting Information), high-rate samples with CsCl exhibited no discernible reduction in inhomogeneity density, which we posit as proof that the observed inhomogeneities arise during deposition.

SEM imaging and EDX were considered to gain further understanding of the nature of these inhomogeneities by analyzing position-dependent bulk material composition. Bulk EDX spectra are similar between 5 and 19 nm min^{-1} samples, see Figure S7 (Supporting Information). However, numerous inhomogeneities are present in SEM images, which likely correspond to the dark PL spots. A representative EDX measurement of such a region is provided in Figure 2c. The halide signals of iodine and bromine are overlaid, showing a small region near the defect of a different material compared to the surrounding bulk. The main dark region exhibits a near complete absence of perovskite with minimal halide and cation presence. As FAI consists of both carbon and nitrogen, the relative absence of nitrogen also precludes these regions as being pure FAI particles, which could have been ejected from the crucible as a spit defect, as has been potentially observed in sequentially sublimated perovskites.[7] What remains is a region of near pure carbon, which is of sufficient relative intensity as to distort the visualization of carbon elsewhere on the bulk sample. Correlation of inhomogeneities with the drop in performance and repeatability observed for deposition rates above 9 nm min^{-1} suggests that the emergence of carbon-rich inhomogeneities may be the cause of reduced performance at higher deposition rates. The bulk crystal structure and overall growth mechanism appear unchanged; therefore, we attribute the reduction in device PCE to these apparent spit defects and seek to identify the cause of these inhomogeneities and the origin of the relatively carbon-rich regions. Interestingly, while these defects reduce device performance, they do not affect long-term MPP stability (Figure S3a, Supporting Information).

2.3. Prevalence of FAI Degradation By-Products for High Deposition Rates

As FAI is known to experience multiple degradation pathways at temperatures within the range used for our systems, we next evaluate if degradation products are expected to negatively impact device PCE. Due to the similar deposition chambers, perovskite precursors and studied deposition rates, we expect that broad conclusions drawn from Process B MS data will be transferrable to Process A. FAI is assumed to dissociate in three distinct pathways, comprised of an initial deprotonation to form formamidine and hydrogen iodide (HI) and further reactions into ammonia

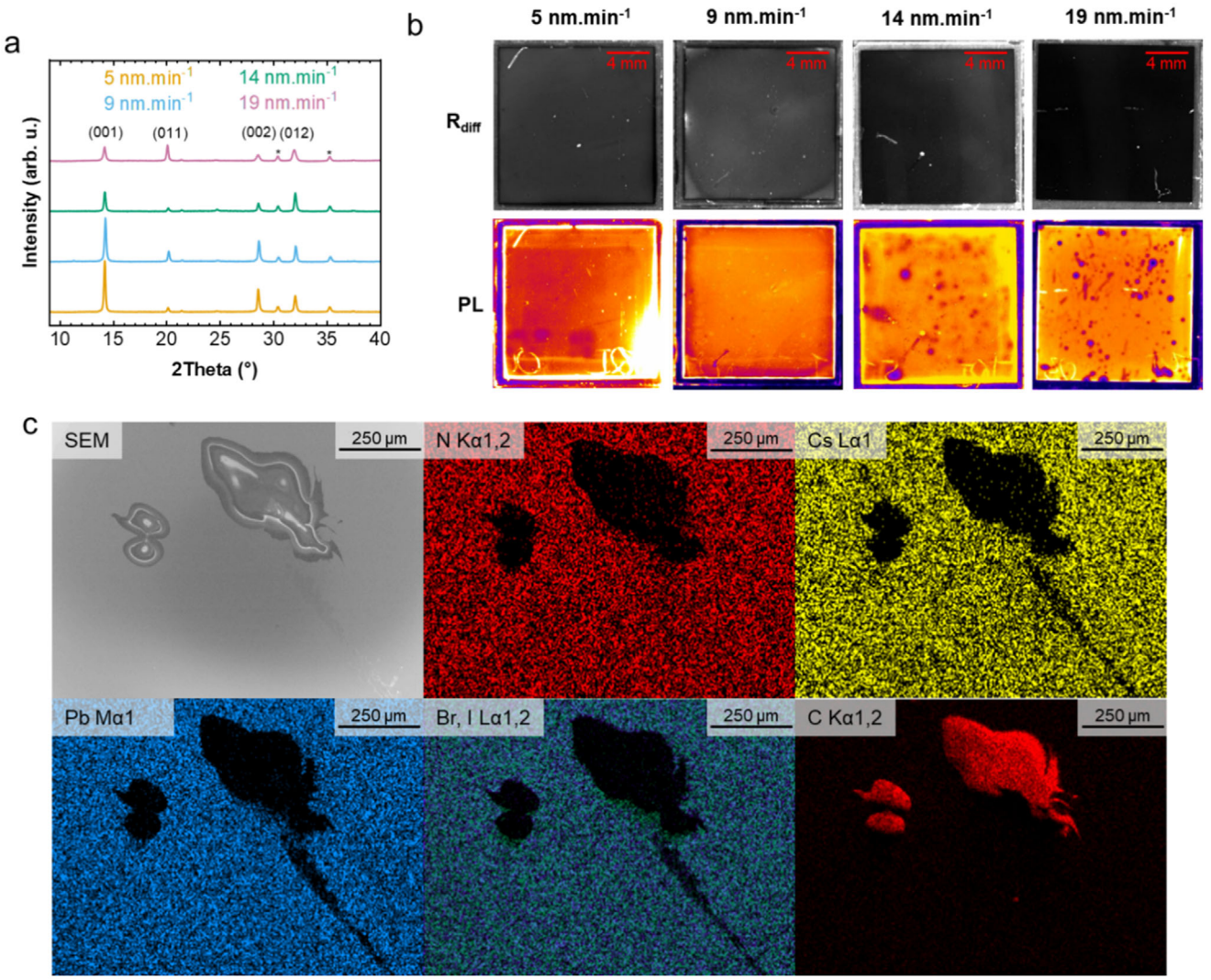

Figure 2. a) XRD spectra of films grown at each studied rate of Process A, with ITO denoted using *. b) Neutral density filter (R_{diff}, top) and normalized PL maps (bottom) of films grown at each studied rate, corresponding to XRD spectra. PL signal was filtered using a longpass 775 nm. c) EDX and SEM data of a representative dark spot, measured on the 19 nm min^{-1} sample in PL mapping. Iodine (blue) and bromine (green) components are overlaid. Carbon is detected outside the carbon-rich region of the EDX spectra, but is not readily apparent due to the high concentration of carbon at the defect.

and either hydrogen cyanide (HCN) or sym-triazine ($C_3H_3N_3$). The formation of sym-triazine typically associated to irreversible material decomposition,[48,60–62] however recent work has suggested this process may be reversible.[63] Similarly, there is not yet consensus on whether the formation of hydrogen cyanide from dissociation of formamidine is reversible, or if other decomposition pathways exist.[35,48,60–62] For simplicity, and the purpose of this work, we will refer to all such materials as degradation products.

MS data for baseline and elevated FAI evaporated rates during Process B perovskite deposition, shown in **Figure 3**, reveal trends in sublimation behavior. Resultant devices for the baseline and 21 nm min^{-1} deposition rates of Process B are shown in a later section. MS measurements were taken during perovskite depositions at the rates provided in the top left of each spectrum. The FAI source shutter was open during the heating process and the reference line indicates when the substrate shutter opens. We note that the FA^+ signal (m/z = 45) drops in the first minutes of the process, which was unexpected.[48] We suspect that FA^+ reacts with inorganic materials within the reactor space, as has been previously theorized for co-evaporated MA-based perovskites.[15] MS signals that remain represent the expected formation of HCN / CNH_2^+, $C_3H_3N_3$ and HI. It is important to consider that the measured degradation products could be the result of FA^+ traversing the ionization zone of the MS system. If this was the explanation for our observations, it is expected tol result in a linear relation between degradation products and FAI deposition rate. We do not observe such a relation between deposition rate and product signals, but insteadobserve substantial changes in degradation products over the course of a reaction with a consistent FAI rate. Hence, while ionization induced degradation of FA^+ molecules could be partially responsible for the detected products, we do not consider it an explanation for the observed trends.

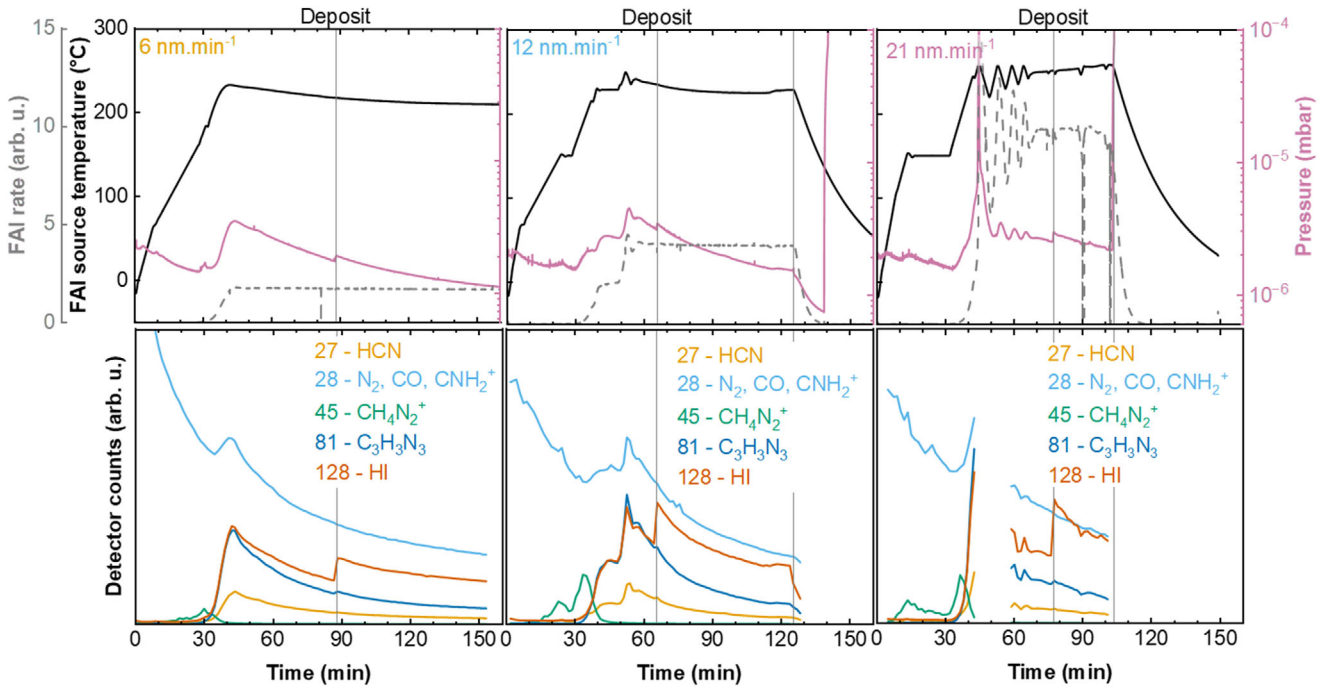

Figure 3. Mass spectroscopy measurements of FAI-based products during Process B perovskite deposition at deposition rates equivalent to 6, 12, and 21 nm min^{-1}. The top row shows the source temperature, reactor pressure and deposition rate, and the bottom row presents the corresponding detector counts. The vertical grey line marked 'Deposit' indicates when the shutter opens and perovskite deposition begins, and the second vertical grey line indicates the end of the process. Due to the extended deposition time for the 6 nm min^{-1} process, the measured interval did not encompass the entire deposition and only one line is shown.

Four key observations are found in our MS data. First, we observe reactor pressure is strongly correlated to the detector counts of each product, which is as expected. Consensus considers it unlikely that degradation products incorporate into the bulk perovskite material in detectable quantities.[35,48,63] Even in the absence of incorporation, co-evaporation at high pressures leads to a reduced mean free path of all materials, which is considered to be incompatible with high-quality perovskite crystal growth.[15,48] Second, we observe a significant increase in the HI-signal (m/z = 128) in the moment the substrate shutter opens. This might be attributed to a special feature of the deposition chamber (Figure S8, Supporting Information), consisting of a cooled enclosure in which potentially degradation products can build up a higher partial pressure. When the substrate shutter opens the HI can escape from this enclosure and reach the mass spectrometer. Next, we note that the m/z = 28 signal decreases before perovskite deposition begins, which is correlated to the falling pressure. The signal appears immediately when the sources are heated and subsequently descreases, which can potentially be attributed to the formation of initial degradation products, such as HCN/CNH_2^+. As CO, N_2 and CNH_2^+ have the same mass, it is difficult to distinguish between them by MS. It is therefore also possible that the signals are caused by gases, such as CO and N_2, trapped in the powder that outgas at low source temperatures. Finally, we do not observe a correlation between high rates and a substantial increase in the presence of degradation products. While detection of sym-triazine and HCN/CNH_2^+ increases when increasing the rate from the baseline 6 nm min^{-1}, their detection is not linearly correlated to the overall deposition rate and is similar for 12 and 21 nm min^{-1} samples. Hence, we can assume that the decreased performance and uniformity at high deposition rates are not due to an increased relative concentration of these degradation products.

2.4. Residual Crucible Material Decomposition for High Deposition Rates

Another potential option to explain the observed sample inhomogeneities is that the residual crucible material substantially changes during the process. To investigate this, we analyzed residual crucible material from Processes A and B using a combination of ^{1}H-NMR and XPS to determine changes in chemical environment. Even at relatively low rates for both Process A and Process B, FAI undergoes a color change. The slight yellowing observed can potentially be attributed to the presence of iodide,[35] which would indicate that not all HI detected in Figure 3 is volatized during sublimation. We also observe clear evidence of decomposition into a black coke substance in the residual crucible material of FAI for higher rates of Process A, as shown in **Figure 4a**. A similar material is present in residual crucible material from Process B high-rate depositions. This black coke substance is a different decomposition product to the previously detected MS degradation products of HCN/CNH_2^+ and sym-triazine, which are not present in the NMR spectrum as they have been volatized.[63] Based on the detected carbon-rich regions in the EDX of our high-rate samples, we consider it likely that fragments of this carbon residue are deposited on

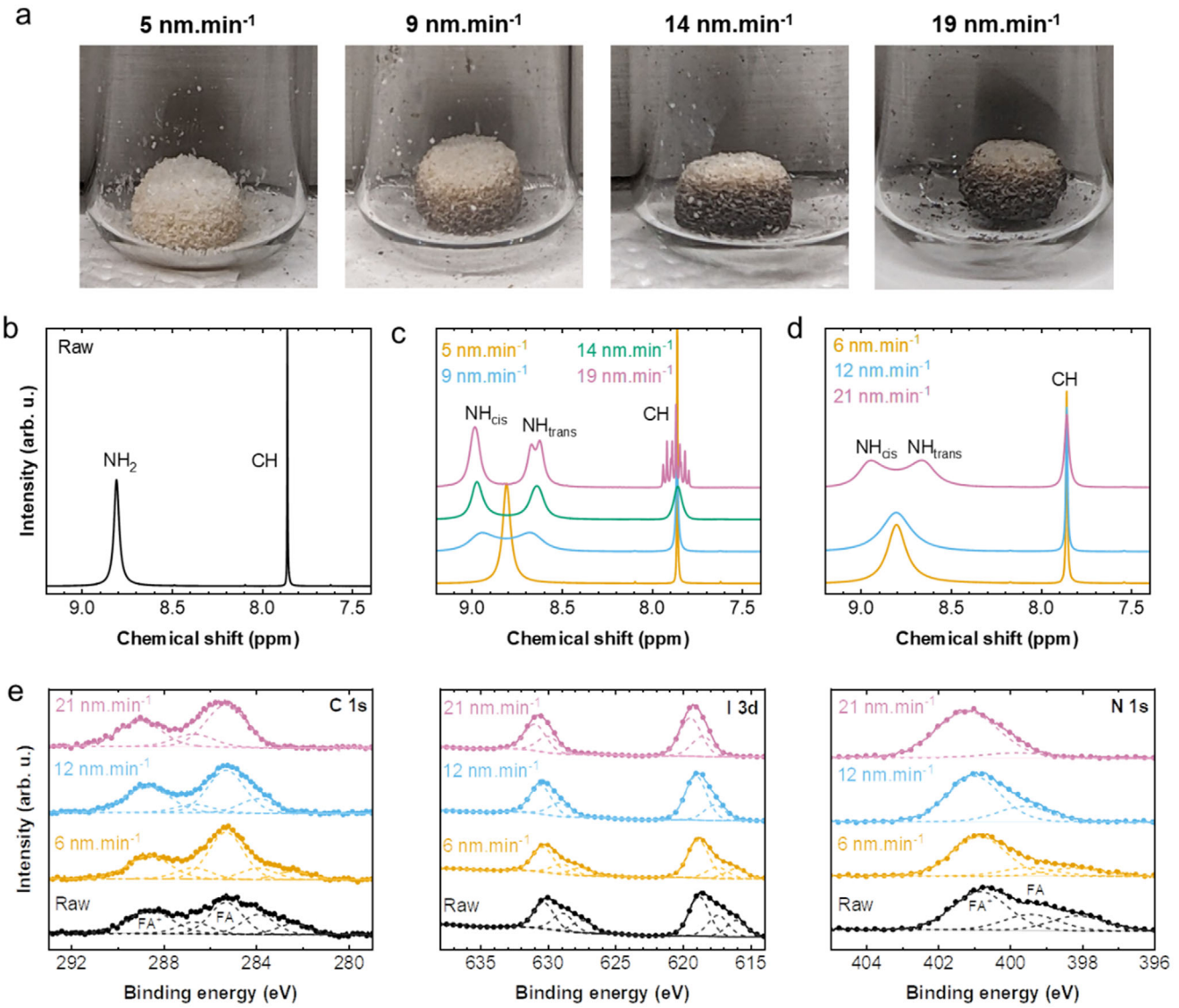

Figure 4. a) Images of residual crucible material at various perovskite deposition rates from Process A. b) ^{1}H-NMR spectrum of raw FAI powder that has not been used for a deposition. c) ^{1}H-NMR of residual crucible material from FAI evaporated at various rates in conical crucibles using Process A, corresponding to the images in a). d) ^{1}H-NMR of residual crucible material from FAI evaporated at various rates in cylindrical crucibles using Process B. e) XPS results of FAI powder before and after deposition at each shown rate in d), as well as a raw powder corresponding to the NMR result shown in b).

the samples at high rates, inhibiting perovskite formation and leading to non-uniform regions. The precise defect deposition method is unknown, it is likely to be a spit defect based on the relatively large particle size. Recent studies on FAI decomposition via quartz tube sublimation report on coke formation at temperatures above 240 °C, indicating that we may experience uneven temperatures within our crucibles.[35] A cross section of a 14 nm min^{-1} residual material puck is presented in the Supporting Information, Figure S9 (Supporting Information), providing evidence of uneven decomposition throughout the material. We assume this is the result of material on the edge of the crucible experiencing higher temperatures than the sublimating bulk material, leading to a region of comparatively higher decomposition.

To analyze material degradation, we compared ^{1}H-NMR spectra of solutions of 30 mg residual crucible material dissolved in 0.6 mL d_6-DMSO (referred to as ≈0.29 M), selected from each studied deposition rate, with a reference of raw powder, shown in Figure 4b,c. ^{1}H-NMR spectra of residual crucible material do not show evidence of the black coke material, which is expected as it was insoluble in d_6-DMSO. Any undissolved material will slightly change the relative concentration of FAI in NMR measurements for high-rate samples as it cannot be separated from the dissolving FAI material but still contributes to the measured mass.

The ^{1}H-NMR peak at 8.80 ppm, corresponding to the amidine moiety, exhibits peak splitting for deposition rates above 9 nm min^{-1}, increasing with respect to sublimation

rate, which has been associated with the presence of acidic compounds.[50,64,65] The absence of doublets for the NH_{trans} peak, with the exception of the Process A 19 nm min^{-1} spectrum, is attributed to the high exchange rate for spin-spin coupling preventing it from being detected at lower rates. Hydrogen bonding, such as is expected for acidic compounds, can depress J-coupling constants.[66,67] Potentially, at 19 nm min^{-1} there is sufficient interaction material for J-coupling to be resolved, splitting the NH_{trans} peak at ≈8.6 ppm into a doublet.

A likely residual material to cause such splitting is HI, and literature on HI splitting of FA-based perovskites reveals a similar peak split as observed for the 19 nm min^{-1} residual material from Figure 4c by exposing the perovskite to ≈10 mM HI.[65] To test this, we exposed a ≈0.29 M raw FAI solution to aqueous HI solution, with the results provided in Figure S10 (Supporting Information), along with controls with and without equivalent pure water exposure. The tested level of water exposure is sufficient to cause relative splitting comparable with 9 nm min^{-1} residual material from Process A, with merely 1 mM HI solution causing splitting equivalent to our 19 nm min^{-1} residual material, providing evidence that HI can cause peak splitting as observed in our high-rate samples. However, a quantitative analysis of relative HI presence is impossible due to the water-induced peak splitting. As the water peak intensity is relatively consistent between rates and is substantially lower for samples without intentional addition of water, we do not consider water to be the primary cause of the observed splitting for other spectra.

To confirm that changes in relative concentration are not the cause for our peak splitting, we also performed ^{1}H-NMR measurements comparing 600 mg in 0.6 mL d_6-DMSO with a ≈0.29 M dilution of this stock solution, presented in Figure S10 of the Supporting Information. These samples do not show changes in peak shape for higher concentrations, only a shift in peak position, as we reported in our previous work.[50]

No additional carbon-containing compounds are observed in the ^{1}H-NMR spectra, consistent with previous reports that symtriazine and HCN are volatized during FAI deposition. Furthermore, if contaminants exist, they would be expected to be present in trace amounts. For this reason, ^{1}H-NMR was also taken of 300 mg FAI in 0.6 mL d_6-DMSO solutions for raw, vacuum-exposed, 5 and 14 nm min^{-1} residual crucible material in order to reveal potential contaminants. A plethora of new peaks are detected in the H_2O region (see Figure S10, Supporting Information), which remain in samples exposed to high vacuum (10^{-6} mbar) for 12 h, indicating that vacuum exposure is insufficient to remove such contaminants. Precise identification of such impurities is non-trivial due to water and acid contamination causing peak shifts. We can attribute some peaks to acetic acid (1.87 ppm singlet) and diethyl ether (1.04 ppm triplet), previously mentioned in literature as steps in FAI fabrication.[68,69] These peaks are consistently not present in the measurements of residual crucible material and are unlikely to be due to sample contamination during the NMR measurement. Hence, controlled sublimation at a low rate is a recommended treatment method to remove such contaminants.

To demonstrate that the observed NMR spectra changes are comparable across different evaporation systems, Figure 4d shows the additional ^{1}H-NMR spectra of residual crucible material from Process B, corresponding to the MS data presented in Figure 3. These materials were evaporated from a 1 cm^3 cylindrical crucible instead of the 8 cm^3 conical crucible of Process A, but the initial precursor material was comparable. Interestingly, the rate-dependent ^{1}H-NMR trend of Process B is offset from the Process A conical ^{1}H-NMR spectra, with the 21 nm min^{-1} Process B measurement being more similar to the 9 nm min^{-1} deposition than the 19 nm min^{-1} of Process A, despite the roughly comparable perovskite deposition rates. We attribute this to the crucible shape improving effective thermal conductivity by increasing the surface area of powder exposed to the crucible, and note we see a reduction in average sublimation temperature for a given sublimation rate.[49] Recreating high-rate spectra using 10 cm^3 cylindrical crucibles in Process A, presented in Figure S11 (Supporting Information), reveals a similar trend in the offset to Process B. The puck of residual material from a cylindrical crucible with ≈40 nm min^{-1} equivalent FAI rate of Process A, shown in Figure S9 (Supporting Information), shows a reduction in both coke formation and material inhomogeneity. These results demonstrate that the degradation associated with high FAI sublimation rates will occur for different crucible shapes, but that the level of coke formation is significantly impacted by crucible shape. This reinforces the need to tailor crucible designs for replicable and reproducible high-rate processes.[49]

XPS measurements of residual crucible material from Process B corresponding to each rate and a raw material reference are presented in Figure 4e. Peak positions of FAI are mostly consistent with those provided in previous literature,[70–72] however, small additional peaks on the lower binding energy side of the main peaks for the raw material are yet unexplained. We believe these peaks belong to residues from FAI synthesis as observed in ^{1}H-NMR spectroscopy. This effect is most clear in the N 1s spectra, where residual peaks that we assign to impurities initially comprise 44.8% of the total N 1s area. With increasing deposition rates and correspondingly higher crucible temperatures, the intensity of the additional peaks decreases, indicating that the amount of synthesis impurities is reduced. For the residual material of the 22 nm min^{-1} process, almost no additional peaks are present in the C 1s, I 3d, and N 1s spectra, with a reduction in relative area to 9.8%. A slightly different picture emerges for the material of Process A as displayed in Figure S12 (Supporting Information). Here, the purification effect seems to be accompanied by decomposition of the FAI. Similar to Process B material, the intensity of the impurity peaks decreases slightly for 5 nm min^{-1} processes compared to the raw material, comprising 42.8% of the N 1s region. For 19 nm min^{-1} deposition rates the intensity of the main peak is reduced and a pronounced shoulder is formed, especially in the I 3d and N 1s spectra, leading to impurity assigned peaks comprising 47.9% of the N 1s spectrum. We attribute these changes to the decomposition of FAI, which we have already observed in the formation of HI via ^{1}H-NMR spectroscopy. Overall, the XPS measurements of representative powders reinforce the differences between Process A and B at high rates observed in ^{1}H-NMR spectroscopy results.

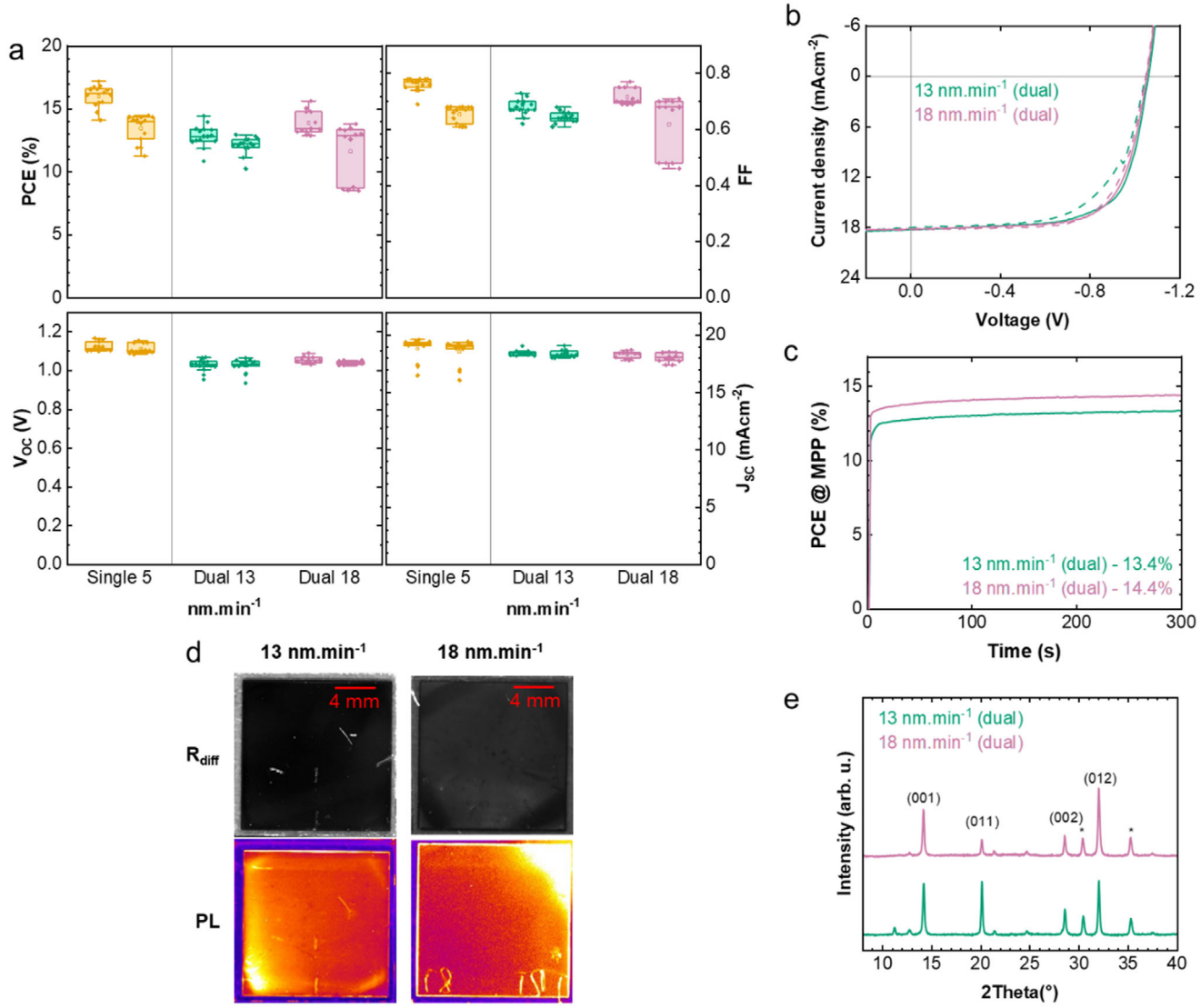

Figure 5. a) Statistics of optimized devices from Process A under various evaporation rates using two FAI sources (labeled as dual), compared to the single FAI source 5 nm min^{-1} baseline shown in Figure 1 (labeled as single). Also shown are b) *J–V*, c) MPP, d) R_{diff} and PL map and e) XRD results corresponding to the champion device. As before, PL signals are normalized. Each condition shows 4 substrates with typically 4 pixels each (active area 10.5 mm^2).

2.5. Increasing Deposition Rates via Utilizing a Dual Source Design

With the cause of variations in device performance identified as tied to FAI sublimation, we consider a modified source setup as a potential method to avoid the increased material decomposition and spit defect formation in high-rate perovskite depositions. The simplest form is to utilize two organic cation sources. We consider two dual FAI source rates, with inorganic sublimation rates comparable to our 14 and 19 nm min^{-1} single FAI source depositions. As the aim was to achieve a direct comparison with Process A single source results, higher deposition rates were not considered, and we continue to utilize conical crucibles. Dual FAI source depositions resulted in a slight reduction of final film thickness (from an average of 560 nm to an average of 500 ± 20 nm); hence, the stated deposition rates for these samples (13 and 18 nm min^{-1}) are slightly lower than reported for single FAI source depositions with comparable inorganic sublimation rates (14 and 19 nm min^{-1}). Statistics of the relevant devices compared to a baseline from Figure 1 are shown in **Figure** 5a, with *J–V* curves and MPP data in Figure 5b,c, respectively.

Some 18 nm min^{-1} samples demonstrated increased hysteresis, as shown in Figure S13 (Supporting Information). Hence, the champion device reached a PCE of 14.0% (FF = 0.71, V_{OC} = 1.06 V, and J_{SC} = 18.5 mA cm^{-2}). Like the single source results, dual source samples remained stable under MPP, with a stabilized PCE at MPP of 14.8% for 18 nm min^{-1} samples, after an initial increase due to light soaking,[73] representing an 8%$_{rel}$ drop in PCE compared to baseline samples, a substantially lower drop

than for single FAI source high-rate samples. Extended MPP tracking for 250 h also yielded stable device performance, similar to the single source devices (Figure S3b, Supporting Information). EQE data is provided in Figure S2 (Supporting Information). Dual FAI source high-rate samples are uniform under PL mapping, as shown in Figure 5d, demonstrating the feasibility of utilizing alternative reactor layouts to increase deposition rate without a decrease in uniformity. Relevant XRD, shown in Figure 5e, display a reduced shift in relative intensity of the (0 0 1) peak compared to equivalent single source baseline and elevated samples, as was shown in Figure 2a. Furthermore, process and performance repeatability improve with a CV_{mean} of 0.082 as shown in Figure S14 (Supporting Information). We note that later batches utilized SnO_x instead of BCP, which may have impacted the absolute value of CV_{mean}. Representative SEM images of 18 nm min^{-1} and baseline 5 nm min^{-1} samples are provided in Figure S15 (Supporting Information). Hence, while employing a dual FAI source design mitigates high-rate losses compared to equivalent-rate single FAI source depositions, some loss in PCE is expected, contrary to rate-dependent performance in MA-based co-evaporated perovskite cells.[45]

2.6. Material Preconditioning as a Method to Improve High Deposition Rates

We also consider FAI preconditioning during the deposition as an alternative method to minimize spit-defect formation in Process B. For a baseline deposition rate of 6 nm min^{-1}, increasing deposition rate to 27 nm min^{-1}, without any applied preconditioning, leads to a similar marked decrease in maximum achievable PCE as observed for Process A, as shown in **Figure 6a**, with corresponding *J–V* curves in Figure 6b. This was despite Process B using a cylindrical crucible, which results in reduced ^{1}H-NMR peak splitting and less observed coke formation at the tested rate compared to the Process A conical crucible at similar rates. Process B also displays a marked decrease in lateral homogeneity of the perovskite films, as measured by PL mapping, with an additional substantial change in XRD pattern when transitioning to high deposition rates. We also observed higher initial pressures as compared to Process A, with a representative deposition pressure curve provided in Figure S16 (Supporting Information), which may impact perovskite formation.[15] Finally, Process B exhibits increased rate-dependent bandgap variation compared to Process A, as evident in the EQE-derived bandgaps shown in Figure S17 (Supporting Information).

To address these issues, we propose an alternative potential method to improve performance, which entails preconditioning the FAI residual material at the desired sublimation rate and maintaining that rate until pressure decreases to a desired value. A representative comparison of pressure curves is shown in Figure S16 (Supporting Information). Such preconditioning achieves three goals: It ensures the removal of all contaminants shown in Figure S10 (Supporting Information), avoids the initial high fractions of degradation products, and finally, avoids the initial high pressure we consider is likely the result of the outgassing from these materials as seen in Figure 3.[35,48]

High-rate perovskites deposited using this method achieved comparable device performance to dual FAI source perovskites employing Process A, and a substantial increase in device performance compared to equivalent-rate perovskites deposited in the same reactor without preconditioning. At the Process B base deposition rate of 6 nm min^{-1}, we obtained a champion PCE of 17.5% (FF = 0.75, V_{OC} = 1.09 V, and J_{SC} = 21.3 mA cm^{-2}) in the reverse scan direction. At increased rates, performance decreases similar to Process A, with the champion device deposited at 27 nm min^{-1} displaying a champion PCE of 11.0% (FF = 0.73, V_{OC} = 1.05 V, and J_{SC} = 14.3 mA cm^{-2}) coupled with significantly increased hysteresis. Preconditioning improves these values, with the champion device deposited at 21 nm min^{-1} displaying a champion PCE of 12.9% (FF = 0.71, V_{OC} = 1.05 V, and J_{SC} = 17.4 mA cm^{-2}) but hysteresis is not significantly reduced and EQE mismatch is within 7%. The relative loss in device PCE is reduced from 31%$_{rel}$ to 26%$_{rel}$ utilizing this method. Differences in deposition rates between preconditioned and non-preconditioned high-rate samples are attributed to changes in final perovskite thickness, not in measured sublimation rate, likely due to the different optimum FAI rates corresponding to the best performance. Representative SEM images of all samples are provided in Figure S18 (Supporting Information). There is clear evidence of smaller grains for the 27 nm min^{-1} sample without preconditioning, especially within the bulk film. This is consistent with structure zone growth models where process pressure is considered, as impurities can lead to spontaneous formation of grain boundaries.[74] Small grains are insufficient to explain performance differences for Process B samples, as baseline Process A samples shown in Figure S15 (Supporting Information) exhibit similar grain sizes without a drop in PCE. Process A grain sizes are attributed to differences in the evaporation chamber setup and the inherent difficulty of accurate pressure measurement within the process chamber.[48] These results indicate that the presence of FAI degradation products can have an impact on film formation by increasing process pressure even if they do not incorporate in the bulk perovskite in detectable quantities.[63]

The bandgap of high-rate Process B samples appeared unaffected by preconditioning. PL maps of high deposition rate perovskites also show an increase in sample homogeneity when preconditioning of the FAI source is performed. As before, PL intensity is normalized for each sample as sample homogeneity is of greater importance than PL intensity for these experiments. The XRD patterns at elevated deposition rates, present in Figure 6d, deviate less strongly compared to the baseline process, whereby the intensity of the (0 0 1) peaks decreases significantly, similar to Process A. However, this is accompanied by a reduction in the PbI_2 peak, and no notable increase in secondary peaks can be observed.

To demonstrate that the effect of this method is process resilient, PL map samples were also fabricated using Process A with both a conical and a cylindrical FAI crucible. Comparing PL maps of samples with and without preconditioning from both processes, as shown in Figure S19 (Supporting Information), indicates that while preconditioning can reduce inhomogeneity density, it is not guaranteed. PL maps for samples grown with the dual FAI source process show a similar improvement in homogeneity for Process B. PL maps of elevated rate Process A samples with preconditioning and conical crucibles continue to display evidence of spit defects, indicating that preconditioning alone will not prevent such defects. However, combining

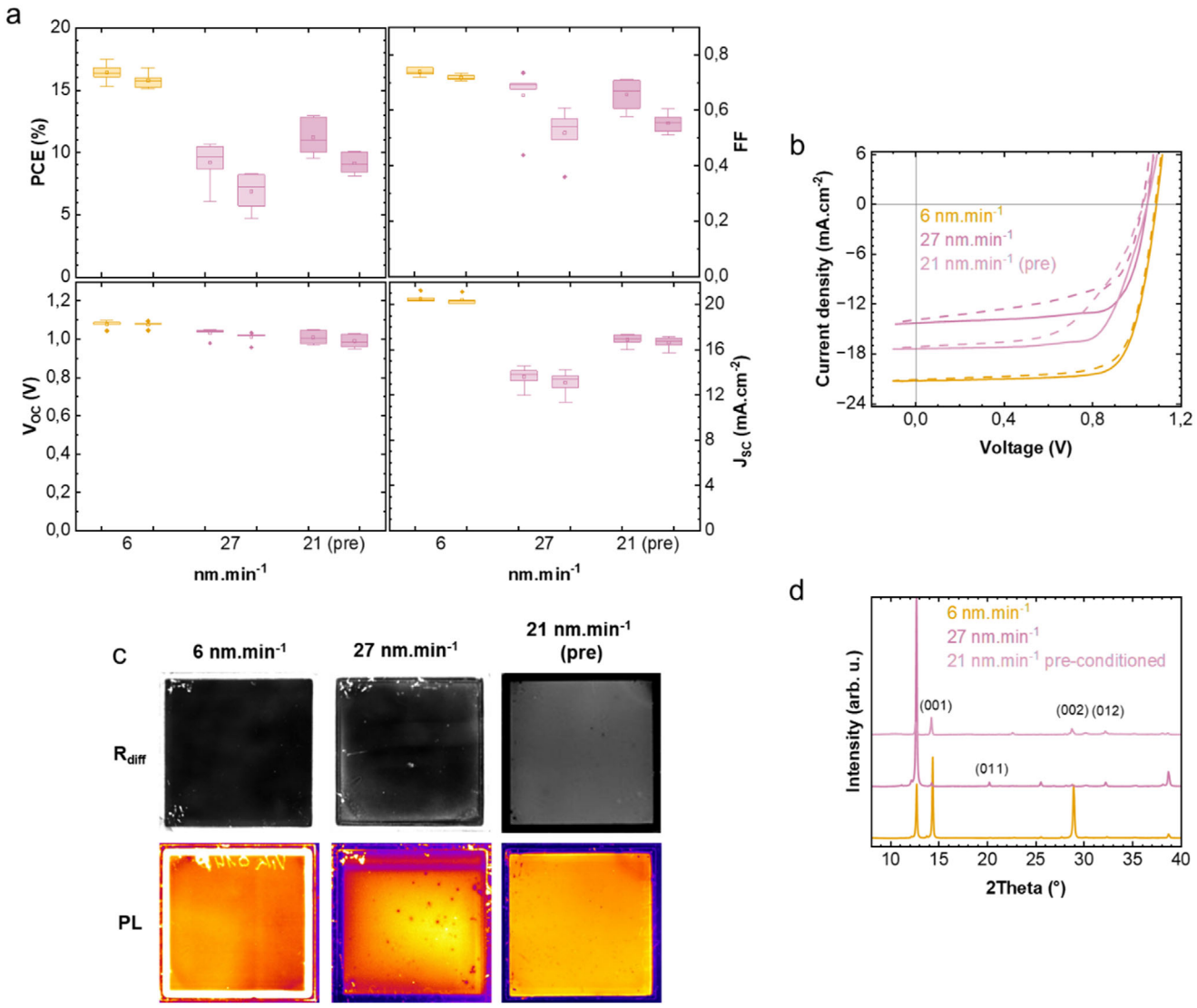

Figure 6. a) Statistics of optimized devices from Process B under a baseline (6 nm min^{-1}) and elevated (21/27 nm min^{-1}) evaporation rate with and without a preconditioning step. The difference in deposition rate for the high-rate samples are due to changes in the final perovskite thickness. Inorganic evaporation rates did not change between 27 and 21 nm min^{-1} (pre). Also shown are b) *J–V*, c) PL map, and d) XRD results corresponding to the champion devices. Each condition provides 2 (27 nm min^{-1}) or 4 (6 and 21 nm min^{-1}) substrates with typically 6 pixels each (active area 17.2 mm^2).

preconditioning with cylindrical crucibles prevents spit defects at high rates, reinforcing our theory that crucible shape is also vital for controlling sample homogeneity at high deposition rates. Such results reveal the need to tailor high-rate deposition methods to the specifics of the reactor and available crucibles. Cylindrical crucibles are preferred as they lead to reduced inhomogeneities and residual material decomposition at high rates.[49]

Samples with effective deposition rates of 54 nm min^{-1} were also fabricated using this preconditioning method, as shown in Figure S20 (Supporting Information). The substantial drop in PCE for these samples indicates that some limitations remain for our proposed method, but this result serves as a proof-of-concept, indicating that such high deposition rates are possible.

3. Conclusion

In this work, we explore the potential for increasing the deposition rate of co-evaporation processes for wide bandgap FA-based perovskite absorbers in two research laboratories with comparable baselines in terms of performance and bandgap. For Process A, we note a 23%$_{rel}$ decrease in performance when increasing deposition rate from 5 nm min^{-1} (16.2%) to 19 nm min^{-1} (12.5%) coupled with a decrease in process repeatability. Material analysis reveals small changes in relative XRD signal intensity and a much larger decrease in sample uniformity, measured by PL mapping. EDX measurements of these samples reveals the cause of the inhomogeneity to be carbon fragments. Process B shows a similar decrease in performance of 31%$_{rel}$ when increasing

deposition rate from 6 nm min^{-1} (17.5%) to 27 nm min^{-1} (11.0%).

Using in-situ MS measurements of the residual gas in the reactor during Process B at various rates, we find no notable change in degradation products for even the highest deposition rate. However, analysis of residual crucible material reveals key changes upon sublimation at high rates. First is the formation of a coke substance on the FAI surfaces touching the crucible, which we consider to be the origin of the carbon fragments observed in high-rate samples. The prevalence of coke and correlated presence of spit defects in perovskite films is found to be dependent on both crucible shape and deposition rate. Observed ^{1}H-NMR peak splitting of the primary FAI peaks is correlated to perovskite deposition rate and is revealed to be due to HI contamination of residual crucible material. We also observe minor impurities in the as-received FAI precursor from the manufacturing process, which are removed upon sublimation.

We explored two methods to overcome the observed rate limitations. Process A utilizes a second cation source to reduce effective FAI sublimation rate. Equivalent high-rate samples with a second FAI source demonstrate an increase in sample uniformity, process repeatability and overall device performance. These improvements reduce the PCE loss to only 8%$_{rel}$ for samples deposited at a rate of 18 nm min^{-1} (14.4%). Process B performs a thermal preconditioning of the FAI to reduce chamber pressure prior to deposition and to ensure that initial contaminants have outgassed. This treatment leads to an increase in sample uniformity and reduces PCE loss to 26%$_{rel}$ for samples deposited at a rate of 21 nm min^{-1} (12.9%). A literature overview together with data from this work is shown in Table S1 (Supporting Information), including the previous fastest FA-based co-evaporated rate of 10 nm min^{-1} (16.6% with a bandgap of 1.58 eV).[75]

Thus, this work provides a comprehensive overview of the limitations for high-rate FA-based co-evaporated perovskites and reveals the mechanisms that can lead to lower solar cell performance. While our achieved deposition rates (18/21 nm min^{-1}) have not approached industrial levels (≈500–1000 nm min^{-1}), we demonstrate the importance of crucible design and provide two methods to remedy the impact on device performance at increased deposition rates. These results are key for the future development of high-rate co-evaporated perovskites.

Supporting Information

Supporting Information is available from the Wiley Online Library or from the author.

Acknowledgements

This work was partly carried out with the support of the Karlsruhe Nano Micro Facility (KNMF) (www.kit.edu/knmf), a Helmholtz Research Infrastructure at Karlsruhe Institute of Technology (KIT). The authors gratefully acknowledge financial support by the Helmholtz Association (program-oriented funding phase IV, MTET Topic 1, Code: 38.01.03; Solar Technology Acceleration Platform (Solar TAP)), the Helmholtz European Partnering Program (TAPAS), the Helmholtz Energy Materials Foundry, the German Federal Ministry for Economic Affairs and Climate Action (BMWK) through the 27Plus6 project (03EE1056B) and the SHAPE project (03EE1123 A-E), the German Federal Ministry of Education and Research (BMBF) through the Zeitenwende Energy Security project and the Ministry of Science and Culture in the State of Lower Saxony through the program "zukunft.niedersachsen" (project NextGenPV). The authors acknowledge support by the Karlsruhe School of Optics & Photonics (KSOP) and the Ministry of Science, Research and Arts of Baden-Württemberg as part of the sustainability financing of the projects of the Excellence Initiative II. This work was partially funded by the European Union. Views and opinions expressed are however, those of the author(s) only and do not necessarily reflect those of the European Union or RIA. Neither the European Union nor the granting authority can be held responsible for them. The NEXUS project has received funding from the European Union's Horizon Europe research and innovation program under grant agreement No. 101075330. The authors thank Dr. Andreas Rapp, Despina Savviduo, Tanja Ohmer-Scherrer and Pascal Merten for their support in measuring herein presented NMR data.

Open access funding enabled and organized by Projekt DEAL.

Conflict of Interest

The authors declare no conflict of interest.

Author Contributions

T.F. and A.M. contributed equally to this work. T.F. and A.M. independently conceived the initial idea for this study and refined it through discussion and collaboration with P.F. and M.R. T.F. fabricated Process A thin-film samples, performed and analyzed relevant J–V, EQE, MPP and XRD measurements and analyzed PL mapping measurements. A.M. fabricated Process B thin-film samples with assistance from V.Š. and S.S., performed and analyzed relevant J–V, EQE, and XRD measurements. A.M. also measured SEM for Process B and EDX for Process A. Together, T.F. and F.L. performed all PL mapping measurements. J.P. performed and analyzed all NMR measurements. A.D. measured all SEM data for Process A. S.M. performed and analyzed all XPS measurements. R.S. measured extended MPP tracking. P.F., M.R, L.K., S.A, and U.W.P. provided valuable discussion and supervised the project. T.F. drafted the manuscript, and the manuscript was written through contributions of all authors. All authors reviewed and commented on the paper.

Data Availability Statement

The data that support the findings of this study are available from the corresponding author upon reasonable request.

Keywords

co-evaporation, co-sublimation, high-rate processes, perovskite solar cells, precursor stability, thermal evaporation, vapor phase deposition

Received: July 11, 2025
Revised: September 5, 2025
Published online:

[1] C. Zuo, H. J. Bolink, H. Han, J. Huang, D. Cahen, L. Ding, *Adv. Sci.* **2016**, *3*, 1500324.
[2] S. De Wolf, J. Holovsky, S.-J. Moon, P. Löper, B. Niesen, M. Ledinsky, F.-J. Haug, J.-H. Yum, C. Ballif, *J. Phys. Chem. Lett.* **2014**, *5*, 1035.
[3] X. Zhao, W. Gao, H. Dong, Y. Zhou, H. Huang, Z. Wu, C. Ran, *Nano Energy* **2024**, *128*, 109933.

[4] M. Saliba, T. Matsui, J.-Y. Seo, K. Domanski, J.-P. Correa-Baena, M. K. Nazeeruddin, S. M. Zakeeruddin, W. Tress, A. Abate, A. Hagfeldt, M. Grätzel, *Energy Environ. Sci.* **2016**, *9*, 1989.
[5] L. Meng, J. You, Y. Yang, *Nat. Commun.* **2018**, *9*, 5265.
[6] R. Singh, H. Hu, T. Feeney, A. Diercks, F. Laufer, Y. Li, T. Duong, F. Schackmar, B. A. Nejand, U. W. Paetzold, *ACS Appl. Mater. Interfaces* **2024**, *16*, 27450.
[7] J. Zhou, L. Tan, Y. Liu, H. Li, X. Liu, M. Li, S. Wang, Y. Zhang, C. Jiang, R. Hua, W. Tress, S. Meloni, C. Yi, *Joule* **2024**, *8*, 1691.
[8] I. Susic, A. Kama, L. Gil-Escrig, C. Dreessen, F. Palazon, D. Cahen, M. Sessolo, H. J. Bolink, *Adv. Mater. Interfaces* **2023**, *10*, 2202271.
[9] T. Feeney, I. M. Hossain, S. Gharibzadeh, F. Gota, R. Singh, P. Fassl, A. Mertens, A. Farag, J.-P. Becker, S. Paetel, E. Ahlswede, U. W. Paetzold, *Sol. RRL* **2022**, *6*, 2200662 .
[10] A. A. B. Baloch, O. Albadwawi, B. AlShehhi, V. Alberts, *Energy Reports* **2022**, *8*, 504.
[11] A. Vossier, F. Gualdi, A. Dollet, R. Ares, V. Aimez, *J. Appl. Phys.* **2015**, *117*, 015102.
[12] S. Rühle, *Sol. Energy* **2016**, *130*, 139 .
[13] I. A. Howard, T. Abzieher, I. M. Hossain, H. Eggers, F. Schackmar, S. Ternes, B. S. Richards, U. Lemmer, U. W. Paetzold, *Adv. Mater.* **2019**, *31*, 1806702.
[14] A. Diercks, J. Petry, T. Feeney, R. Singh, T. Zhao, H. Hu, Y. Li, U. W. Paetzold, P. Fassl, *ACS Energy Lett.* **2025**, *20*, 1165.
[15] T. Abzieher, T. Feeney, F. Schackmar, Y. J. Donie, I. M. Hossain, J. A. Schwenzer, T. Hellmann, T. Mayer, M. Powalla, U. W. Paetzold, *Adv. Funct. Mater.* **2021**, *31*, 2104482.
[16] M. Roß, S. Severin, M. B. Stutz, P. Wagner, H. Köbler, M. Favin-Lévêque, A. Al-Ashouri, P. Korb, P. Tockhorn, A. Abate, B. Stannowski, B. Rech, S. Albrecht, *Adv. Energy Mater.* **2021**, *11*, 2101460.
[17] M. R. Leyden, L. K. Ono, S. R. Raga, Y. Kato, S. Wang, Y. Qi, *J. Mater. Chem A Mater.* **2014**, *2*, 18742.
[18] G. Longo, L. Gil-Escrig, M. J. Degen, M. Sessolo, H. J. Bolink, *Chem. Commun.* **2015**, *51*, 7376.
[19] B. Gao, Z. Zuo, J. Hu, Q. Qi, Z. Peng, S. Hou, Y. Fu, D. Zou, *ACS Mater. Lett.* **2024**, *6*, 5300.
[20] V. Kliner, T. Soto-Montero, J. Nespoli, T. J. Savenije, M. Ledinský, M. Morales-Masis, *J. Phys. Chem. Lett.* **2025**, *16*, 1453.
[21] N. Rodkey, I. Gomar-Fernández, F. Ventosinos, C. Roldan-Carmona, L. J. A. Koster, H. J. Bolink, *ACS Energy Lett.* **2024**, *9*, 927.
[22] Q. Guesnay, F. Sahli, C. Ballif, Q. Jeangros, *APL Mater.* **2021**, *9*, 100703.
[23] F. Sahli, J. Werner, B. A. Kamino, M. Bräuninger, R. Monnard, B. Paviet-Salomon, L. Barraud, L. Ding, J. J. Diaz Leon, D. Sacchetto, G. Cattaneo, M. Despeisse, M. Boccard, S. Nicolay, Q. Jeangros, B. Niesen, C. Ballif, *Nat. Mater.* **2018**, *17*, 820.
[24] O. Er-raji, M. A. A. Mahmoud, O. Fischer, A. J. Ramadan, D. Bogachuk, A. Reinholdt, A. Schmitt, B. P. Kore, T. W. Gries, A. Musiienko, O. Schultz-Wittmann, M. Bivour, M. Hermle, M. C. Schubert, J. Borchert, S. W. Glunz, P. S. C. Schulze, *Joule* **2024**, *8*, 2811.
[25] A. Farag, T. Feeney, I. M. Hossain, F. Schackmar, P. Fassl, K. Küster, R. Bäuerle, M. A. Ruiz-Preciado, M. Hentschel, D. B. Ritzer, A. Diercks, Y. Li, B. A. Nejand, F. Laufer, R. Singh, U. Starke, U. W. Paetzold, *Adv. Energy Mater.* **2023**, *13*, 2203982.
[26] J. B. Patel, A. D. Wright, K. B. Lohmann, K. Peng, C. Q. Xia, J. M. Ball, N. K. Noel, T. W. Crothers, J. Wong-Leung, H. J. Snaith, L. M. Herz, M. B. Johnston, *Adv. Energy Mater.* **2020**, *10*, 1903653.
[27] D. B. Ritzer, T. Abzieher, A. Basibüyük, T. Feeney, F. Laufer, S. Ternes, B. S. Richards, S. Bergfeld, U. W. Paetzold, *Prog Photovolt* **2021**, *30*, 360.
[28] A. Paliwal, K. P. S. Zanoni, C. Roldán-Carmona, M. A. Hernández-Fenollosa, H. J. Bolink, *Matter* **2023**, *6*, 3499 .
[29] F. U. Kosasih, E. Erdenebileg, N. Mathews, S. G. Mhaisalkar, A. Bruno, *Joule* **2022**, *6*, 2692.
[30] T. Abzieher, D. T. Moore, M. Roß, S. Albrecht, J. Silvia, H. Tan, Q. Jeangros, C. Ballif, M. T. Hoerantner, B.-S. Kim, H. J. Bolink, P. Pistor, J. C. Goldschmidt, Y.-H. Chiang, S. D. Stranks, J. Borchert, M. D. McGehee, M. Morales-Masis, J. B. Patel, A. Bruno, U. W. Paetzold, *Energy Environ. Sci.* **2024**, *17*, 1645.
[31] J. Zhang, J. Wu, A. Barabash, T. Du, S. Qiu, V. M. Le Corre, Y. Zhao, K. Zhang, F. Schmitt, Z. Peng, J. Tian, C. Li, C. Liu, T. Heumueller, L. Lüer, J. A. Hauch, C. J. Brabec, *Energy Environ. Sci.* **2024**, *17*, 5490 .
[32] K. P. Goetz, Y. Vaynzof, *ACS Energy Lett.* **2022**, *7*, 1750.
[33] X. Cao, L. Hao, Z. Liu, G. Su, X. He, Q. Zeng, J. Wei, *Chem. Eng. J.* **2022**, *437*, 135458.
[34] D. H. Kim, J. B. Whitaker, Z. Li, M. F. A. M. van Hest, K. Zhu, *Joule* **2018**, *2*, 1437 .
[35] J. Petry, V. Skorjanc, A. Diercks, T. Feeney, A. Morsa, S. R. Kimmig, J. Baumann, F. Löffler, S. Auschill, J. Damm, D. Baumann, F. Laufer, J. Kurpiers, M. Müller, L. Korte, S. Albrecht, M. Roß, U. W. Paetzold, P. Fassl, *EES Solar* **2025**, *1*, 404.
[36] V. Škorjanc, A. Miaskiewicz, M. Roß, S. Maniyarasu, S. Severin, M. R. Leyden, P. Holzhey, F. Ruske, L. Korte, S. Albrecht, *ACS Energy Lett.* **2024**, *9*, 5639 .
[37] C. Peng, B. Chen, X. Liu, R. Guo, Z. He, F. Zhang, X. He, L. Sun, Z. Liu, Y. Xiong, F. Gao, L. Wang, *Chem. Eng. J.* **2024**, *499*, 155955.
[38] S. Han, S. K. Hyeong, S. K. Lee, N. Shin, *Chem. Eng. J.* **2022**, *439*, 135715.
[39] M. R. Leyden, V. Škorjanc, A. Miaskiewicz, S. Severin, S. Maniyarasu, T. Gries, J. Beckedahl, F. Scheler, M. Simmonds, P. Holzhey, J. Kurpiers, L. Korte, M. Roß, S. Albrecht, *Sol. RRL* **2024**, *8*, 2400575.
[40] H. Xu, Y. Wu, F. Xu, J. Zhu, C. Ni, W. Wang, F. Hong, R. Xu, F. Xu, J. Huang, L. Wang, *RSC Adv.* **2016**, *6*, 48851.
[41] M. Tai, X. Zhao, H. Wei, G. Wang, F. Hao, X. Li, X. Yin, Y. Zhou, J. Han, Y. Wei, K. Jiang, H. Lin, *ACS Appl. Mater. Interfaces* **2018**, *10*, 26206.
[42] B. Geffroy, P. le Roy, C. Prat, *Polym. Int.* **2006**, *55*, 572.
[43] N. G. Dhere, *Sol. Energy Mater. Sol. Cells* **2007**, *91*, 1376.
[44] H. A. Dewi, E. Erdenebileg, D. D. Luca, S. G. Mhaisalkar, A. Bruno, *ACS Energy Lett.* **2024**, *9*, 4319.
[45] M. Piot, J. E. S. Alonso, K. P. S. Zanoni, N. Rodkey, F. Ventosinos, C. Roldán-Carmona, M. Sessolo, H. Bolink, *ACS Energy Lett.* **2023**, *8*, 4711.
[46] F. Palazon, D. Pérez-del-Rey, S. Marras, M. Prato, M. Sessolo, H. J. Bolink, L. Manna, *ACS Energy Lett.* **2018**, *3*, 835.
[47] B. Conings, J. Drijkoningen, N. Gauquelin, A. Babayigit, J. D'Haen, L. D'Olieslaeger, A. Ethirajan, J. Verbeeck, J. Manca, E. Mosconi, F. D. Angelis, H.-G. Boyen, *Adv. Energy Mater.* **2015**, *5*, 1500477.
[48] M. Kroll, S. D. Öz, Z. Zhang, R. Ji, T. Schramm, T. Antrack, Y. Vaynzof, S. Olthof, K. Leo, *Sustain. Energy Fuels* **2022**, *6*, 3230.
[49] A. Dierck, J. Petry, T. Feeney, R. Thelen, P. Fassl, U. W. Paetzold, *Adv. Mater. Technol.* **2025**, e01549, https://doi.org/10.1002/admt.202501549.
[50] T. Feeney, J. Petry, A. Torche, D. Hauschild, B. Hacene, C. Wansorra, A. Diercks, M. Ernst, L. Weinhardt, C. Heske, G. Gryn'ova, U. W. Paetzold, P. Fassl, *Matter* **2024**, *7*, 2066 .
[51] A.-F. Castro-Méndez, F. Jahanbakhshi, D. K. LaFollette, B. J. Lawrie, R. Li, C. A. R. Perini, A. M. Rappe, J.-P. Correa-Baena, *J. Am. Chem. Soc.* **2024**, *146*, 18459.
[52] T. Du, W. Xu, S. Xu, S. R. Ratnasingham, C.-T. Lin, J. Kim, J. Briscoe, M. A. McLachlan, J. R. Durrant, *J. Mater Chem. C Mater.* **2020**, *8*, 12648.
[53] M. Saliba, L. Etgar, *ACS Energy Lett.* **2020**, *5*, 2886.
[54] M. Saliba, E. Unger, L. Etgar, J. Luo, T. J. Jacobsson, *Nat. Commun.* **2023**, *14*, 5445.
[55] Y.-H. Chiang, K. Frohna, H. Salway, A. Abfalterer, L. Pan, B. Roose, M. Anaya, S. D. Stranks, *ACS Energy Lett.* **2023**, *8*, 2728.

[56] Y.-Y. Xu, Y. Jiang, H.-Q. Du, X. Gao, Z.-Y. Qiang, C.-X. Wang, Z.-W. Tao, L.-H. Yang, R. Zhi, G.-J. Liang, H.-Y. Cai, M. U. Rothmann, Y.-B. Cheng, W. Li, *Adv. Funct. Mater.* **2024**, *34*, 2312037.
[57] T. J. Jacobsson, J.-P. Correa-Baena, E. Halvani Anaraki, B. Philippe, S. D. Stranks, M. E. F. Bouduban, W. Tress, K. Schenk, J. Teuscher, J.-E. Moser, H. Rensmo, A. Hagfeldt, *J. Am. Chem. Soc.* **2016**, *138*, 10331.
[58] G. Tumen-Ulzii, C. Qin, D. Klotz, M. R. Leyden, P. Wang, M. Auffray, T. Fujihara, T. Matsushima, J.-W. Lee, S.-J. Lee, Y. Yang, C. Adachi, *Adv. Mater.* **2020**, *32*, 1905035.
[59] P. Fassl, V. Lami, A. Bausch, Z. Wang, M. T. Klug, H. J. Snaith, Y. Vaynzof, *Energy Environ. Sci.* **2018**, *11*, 3380.
[60] S. Thampy, B. Zhang, J. G. Park, K. H. Hong, J. W. P. Hsu, *Mater. Adv.* **2020**, *1*, 3349.
[61] L. Ma, D. Guo, M. Li, C. Wang, Z. Zhou, X. Zhao, F. Zhang, Z. Ao, Z. Nie, *Chem. Mater.* **2019**, *31*, 8515.
[62] E. J. Juarez-Perez, L. K. Ono, Y. Qi, *J. Mater. Chem A Mater* **2019**, *7*, 16912.
[63] A. G. Kuba, F. Sahli, M. Othman, K. Artuk, Q. Jeangros, A. Hessler-Wyser, C. Ballif, C. M. Wolff, *ACS Energy Lett.* **2025**, *10*, 2710.
[64] P. Charisiadis, V. Kontogianni, C. Tsiafoulis, A. Tzakos, M. Siskos, I. Gerothanassis, *Molecules* **2014**, *19*, 13643.
[65] W. T. M. Van Gompel, R. Herckens, G. Reekmans, B. Ruttens, J. D'Haen, P. Adriaensens, L. Lutsen, D. Vanderzande, *J. Phys. Chem. C* **2018**, *122*, 4117.
[66] E. Y. Tupikina, G. S. Denisov, A. S. Antonov, P. M. Tolstoy, *Phys. Chem. Chem. Phys.* **2020**, *22*, 1994.
[67] J. E. Del Bene, J. Elguero, *J. Am. Chem. Soc.* **2004**, *126*, 15624.
[68] G. E. Eperon, S. D. Stranks, C. Menelaou, M. B. Johnston, L. M. Herz, H. J. Snaith, *Energy Environ. Sci.* **2014**, *7*, 982.
[69] G. R. Fulmer, A. J. M. Miller, N. H. Sherden, H. E. Gottlieb, A. Nudelman, B. M. Stoltz, J. E. Bercaw, K. I. Goldberg, *Organometallics* **2010**, *29*, 2176.
[70] S. Wang, D. Khan, W. Zhou, Y. Sui, T. Zhang, G. Yu, Y. Huang, X. Yang, X. Chen, H. Yan, J. Tang, F. Yang, P. Han, Z. Zheng, Y. Zhang, Z. Tang, *Adv. Funct. Mater.* **2024**, *34*, 2316202.
[71] R. Das Adhikari, H. Baishya, M. J. Patel, D. Yadav, P. K. Iyer, *Small* **2024**, *20*, 2404588.
[72] L. Qiu, Z. Liu, L. Chen, W.-H. Chen, Y. Yuan, L. Song, B. Bai, P. Du, J. Xiong, *ACS Appl. Nano Mater.* **2023**, *6*, 15408.
[73] L. Lin, L. Yang, G. Du, X. Li, Y.-N. Li, J. Deng, K. Wei, J. Zhang, *ACS Appl. Energy Mater.* **2023**, *6*, 10303.
[74] I. Petrov, P. B. Barna, L. Hultman, J. E. Greene, *J. Vac. Sci. Technol., A* **2003**, *21*, S117.
[75] R. Ji, Z. Zhang, C. Cho, Q. An, F. Paulus, M. Kroll, M. Löffler, F. Nehm, B. Rellinghaus, K. Leo, Y. Vaynzof, *J. Mater. Chem C Mater.* **2020**, *8*, 7725.